Contribution of high-mode near-inertial waves to enhanced typhoon-induced sea surface temperature cooling in the South China Sea

Shukui Cheng [a], Anzhou Cao [a,*], Jinbao Song [a], Xinyu Guo [b]

[a] *Ocean College, Zhejiang University, Zhoushan, China*
[b] *Center for Marine Environmental Studies, Ehime University, Matsuyama, Japan*

ARTICLE INFO

ABSTRACT

Sea surface temperature cooling (SSTC) is an important indicator of the ocean response to typhoons and is a factor in the evolution of typhoons. Understanding the intricate mechanisms underlying the SSTC induced by different typhoons is important. Based on the numerical simulation, we investigated the SSTC induced by typhoons Megi (2010), Linfa (2015), and Sarika (2011), which had relatively similar tracks in the South China Sea. As the strongest (weakest) typhoon, Megi (Sarika) induced the largest (smallest) SSTC, which is consistent with the traditional understanding that stronger typhoons usually induce larger SSTC than weaker typhoons. However, the SSTC induced by the moderate typhoon Linfa was nearly comparable to that induced by Megi, while Linfa had a wind power input an order of magnitude smaller. A comparison of near-inertial waves (NIWs) induced by Linfa and Megi showed that the former contained a larger proportion of high modes, substantially contributing to vertical shear. Consequently, the vertical mixing coefficient during Linfa reached one third of that during Megi. Because the SSTC is primarily influenced by vertical mixing, which is dominated by vertical diffusion at the mixed layer depth, the relatively strong vertical mixing coefficient and large temperature gradient during Linfa ultimately resulted in the SSTC nearly comparable to that induced by Megi. The results of this study enhance the understanding of typhoon-induced SSTC.

1. Introduction

Typhoons are powerful cyclone events that occur over tropical and subtropical oceans in the Northwest Pacific Ocean, often significantly damaging coastal areas. Annually, typhoons and consequential disasters, such as storm surges, heavy rainfall, and massive waves, lead to thousands of fatalities and billions of dollars in economic loss (Li et al., 2020a; Zhang et al.,2021; Tan et al., 2023; Krishnaja et al., 2024; Shi et al., 2024). Therefore, promoting the prediction of a typhoon's track and intensity is important to mitigate the damage caused by typhoons.

During a typhoon, important momentum, heat, and mass exchanges between the ocean and atmosphere influence the upper ocean and typhoons. Typhoons can induce sea surface temperature cooling (SSTC; Price, 1981; Emanuel, 2003). Vertical mixing is the main cause of typhoon-induced SSTC, accounting for more than 75 % of the cooling (Price, 1981; Greatbatch, 1984; Shay et al., 1992; Jacob et al., 2000; Jullien et al., 2012; Qiao et al., 2022). The main driver of enhanced vertical mixing during a typhoon is the vertical shear instability induced by typhoon-induced near-inertial waves (NIWs). Hence, understanding

the generation, propagation, characteristics and dissipation of typhoon-induced NIWs is of great importance (e.g. Shay et al., 1990; 1992; 1998; Shay & Chang, 1997; Rayson et al., 2015; Yang et al., 2015). In addition to vertical mixing, the upwelling induced by typhoon wind stress, which transports colder water from the lower ocean to the upper ocean, constrains the temperature gradient at the mixed-layer base, thereby strongly influencing the SSTC (Price, 1981; Chiang et al., 2011; Jullien et al., 2012). Ocean–atmosphere heat exchange during a typhoon, including weakened solar radiation due to heavy clouds and enhanced evaporation due to strong winds, also impacts the SSTC (Price, 1981; Bender et al. 1993; Huang et al. 2009; Pei et al., 2015).

Typhoon characteristics, including the maximum wind speed, radius of the maximum wind speed, and translation speed, are crucial for SSTC (Lin et al., 2008; 2009; Wang et al., 2016). A larger radius of maximum wind speed and slow translation speed increases the duration of the typhoon at a given point in the ocean and thus tends to increase the SSTC (Pun et al., 2018; Liu et al., 2023). Translation speed further modulates the relative importance of upwelling and vertical mixing in driving SSTC (Lin et al., 2008, 2009; Chiang et al., 2011; Jullien et al., 2012). The

---

maximum wind speed directly affects the intensity of the dynamic processes of SSTC, including vertical mixing and upwelling, which dominate typhoon-induced SSTC (Vincent et al., 2012a; Jullien et al., 2012). Higher maximum wind speeds usually indicate heavier clouds and stronger evaporation. Therefore, stronger typhoons usually induce larger SSTC than weaker typhoons. On average, typhoons with maximum wind speeds above 44 m/s induce approximately twice as much SSTC as those with a maximum wind speed of 17–32 m/s (Dare & Mcbride, 2011; Vincent et al., 2012a; Cui et al., 2023).

Ocean conditions before the arrival of a typhoon also influence typhoon-induced SSTC. Shallow mixed layer depth (MLD), high sea surface temperature (SST), and steep thermocline are advantageous for large SSTCs (Neetu et al., 2012; Vincent et al., 2012b; Guan et al., 2021). A cold core eddy can enhance the typhoon-induced SSTC because it has a shallower MLD and can cause a stronger near-inertial velocity response in the mixed layer, whereas a warm core eddy can weaken the typhoon-induced SSTC (Shay et al. 1992; Wu et al., 2007; Jaimes & Shay, 2010). Furthermore, salinity-induced barrier layers can enhance vertical stratification stability, suppress vertical mixing, and weaken the SSTC (Neetu et al., 2012; Balaguru et al., 2012; Pun et al., 2023).

Because the formation and maintenance of a typhoon rely on the continuous transport of vapor and heat from the upper ocean to the atmosphere, the reduction in upper ocean temperature caused by typhoons also limits its intensity (Schade & Emanuel, 1999; Zhu & Zhang, 2006; Wu et al., 2008). Consequently, SSTC is an important indicator of the ocean response to typhoons and is also a factor in the evolution of typhoons.

The Northwest Pacific Ocean has the highest concentration ($>$30 % per year) of tropical cyclones worldwide (Chan, 2005). As the largest marginal sea in the Northwestern Pacific Ocean, the South China Sea (SCS) is frequently influenced by typhoons. In this study, we chose three typhoons (Megi in October 2010, Linfa in July 2015, and Sarika in June 2011) that had relatively similar tracks but caused different SSTC in the SCS. Megi was a super typhoon, which was the strongest typhoon worldwide in 2010 and the strongest in the Northwest Pacific Ocean between Tip in 1979 and Haiyan in 2013. Several studies have investigated the intense SSTC and NIWs induced by Megi (e.g., Guan et al., 2014; Ko et al., 2014; Cao et al., 2018; Pun et al., 2018; Zheng et al., 2023). Over the SCS Basin, super typhoon Megi, whose maximum wind speed was above 50 m/s, induced the SSTC of approximately 5.09 °C. In contrast, Linfa and Sarika were weak typhoons, with maximum wind speeds of less than 30 m/s. However, Linfa caused a strong SSTC of 4.12 °C, which is almost comparable to that of Megi, whereas Sarika induced a much smaller SSTC of 1.32 °C. According to observation statistics, few typhoons can induce SSTC exceeding 4 °C, and the mean SSTC induced by typhoons with maximum wind speeds of 17–33 m/s is less than 1 °C (Vincent et al., 2012a; Cui et al., 2023). Consequently, exploring the mechanism through which typhoon Linfa caused the SSTC almost comparable to that of super typhoon Megi was the motivation for this study.

The remainder of this paper is organized as follows. The best track dataset of the three typhoons, remote sensing data, and numerical model used in this study are introduced in Section 2. Section 3 describes the data processing methodology. The main results, including the typhoon-induced SSTC, temperature budget in the mixed layer, and typhoon-induced NIWs, are presented in Section 4. The discussion is presented in Section 5. Finally, Section 6 summarizes the study.

2. Data and model

2.1. Data

The characteristics and tracks of typhoons Megi (October 2010), Linfa (July 2015), and Sarika (June 2011) were obtained from the best track dataset of the China Meteorological Administration Tropical Cyclone Data Center (http://tcdata.typhoon.org.cn) (Ying et al., 2014;

Lu et al., 2021). Fig. 1a shows the tracks and corresponding dates of the three typhoons as well as the bathymetry from the 1 arc-minute global relief model (ETOPO1, https://ngdc.noaa.gov/mgg/global/relief/ETOPO1). The three typhoons had relatively similar tracks crossing the SCS basin from south to north. Table 1 lists the maximum wind speed, central pressure, and translation speed of the three typhoons when they passed over the SCS Basin. Among the three typhoons, Megi was the strongest, with a maximum wind speed of 50 m/s. Its central pressure was 940 hPa, and its average translation speed was approximately 3 m/s. Linfa was the slowest, with an average translation speed of approximately 2 m/s. Its maximum wind speed was between 20 and 28 m/s, and its central pressure was between 995 and 985 hPa. Sarika was the weakest and fastest, with a maximum wind speed of 20 m/s and a translation speed of approximately 7 m/s. The central pressure was approximately 995 hPa.

Because of their capacity to penetrate cloud cover, microwave radiometers offer a valuable method for measuring SST during typhoons. Therefore, these SST data were used to investigate the SSTC induced by the three typhoons. The SST data used in this study were downloaded from Remote Sensing Systems (https://www.remss.com/), with a spatial resolution of 9 km and a temporal interval of one day.

2.2. Model configurations

The Coastal and Regional Ocean Community model (CROCO v1.1; https://www.croco-ocean.org; 10.5281/zenodo.7415133) was used. The CROCO is built on the Regional Ocean Modeling System (ROMS_AGRIF) that solves the primitive equations of the ocean. Based on CROCO, numerical experiments were conducted to simulate the ocean response to the three typhoons. Note that this study only focused on the ocean response to typhoons, whereas the ocean feedback on typhoons was not considered.

The model domain was 114.5–124.5° E, 15.5–24.5° N, with a horizontal resolution of 1/20° (approximately 5 km). Fifty uneven sigma layers were set in the vertical direction, with stretching parameters of 15.0 for THETA_S and 0.4 for THETA_B. Bathymetric data were obtained using the ETOPO1 (Fig. 1a). Forcing data, including wind speed 10 m above the sea surface, solar radiation, humidity, precipitation, and air temperature, were derived from the Climate Forecast System Reanalysis dataset (CFSR) downloaded from the Asia-Pacific Data Research Center (https://apdrc.soest.hawaii.edu/). Through a series of controlled experiments, the shortwave radiation data during typhoons Megi and Sarika were adjusted to 0.8 times the raw data to match the SST observational data. Tidal forcing data, containing eight tidal constituents (M_2, S_2, N_2, K_2, K_1, O_1, P_1 and Q_1), were obtained from TPXO7 (Egbert & Erofeeva, 2002). The initial and lateral boundary conditions for the numerical simulations were obtained from the ocean temperature, salinity, and velocity fields derived from the Hybrid Coordinate Ocean Model reanalysis dataset (HYCOM GOFS 3.1, https://www.hycom.org/).

The simulations adopted the bulk calculation of COARE3p0. The K-Profile Parameterization (KPP) vertical mixing scheme (Large et al., 1994) were used in the CROCO. The 3rd-order upstream biased advection scheme was employed for the lateral momentum advection, and a 4th-order compact advection scheme was employed for the vertical momentum advection. The Laplacian background viscosity and diffusivity were 1000 and 100 m^2/s, respectively. A 100-km wide sponge layer with enhanced viscosity and diffusivity was set at the open boundaries to absorb baroclinic energy. The numerical simulations for typhoons Megi, Linfa, and Sarika started on October 8, 2010, June 24, 2015, and May 30, 2011, respectively, approximately 10 days before they entered the SCS. In each simulation, CROCO was operated for 20 days with a baroclinic time step of 120 s, and the number of barotropic time steps within each baroclinic time step was 60. The simulation results were output every 1 h. In the Appendix, the sensitivities of simulated results to model resolution, vertical mixing scheme and output
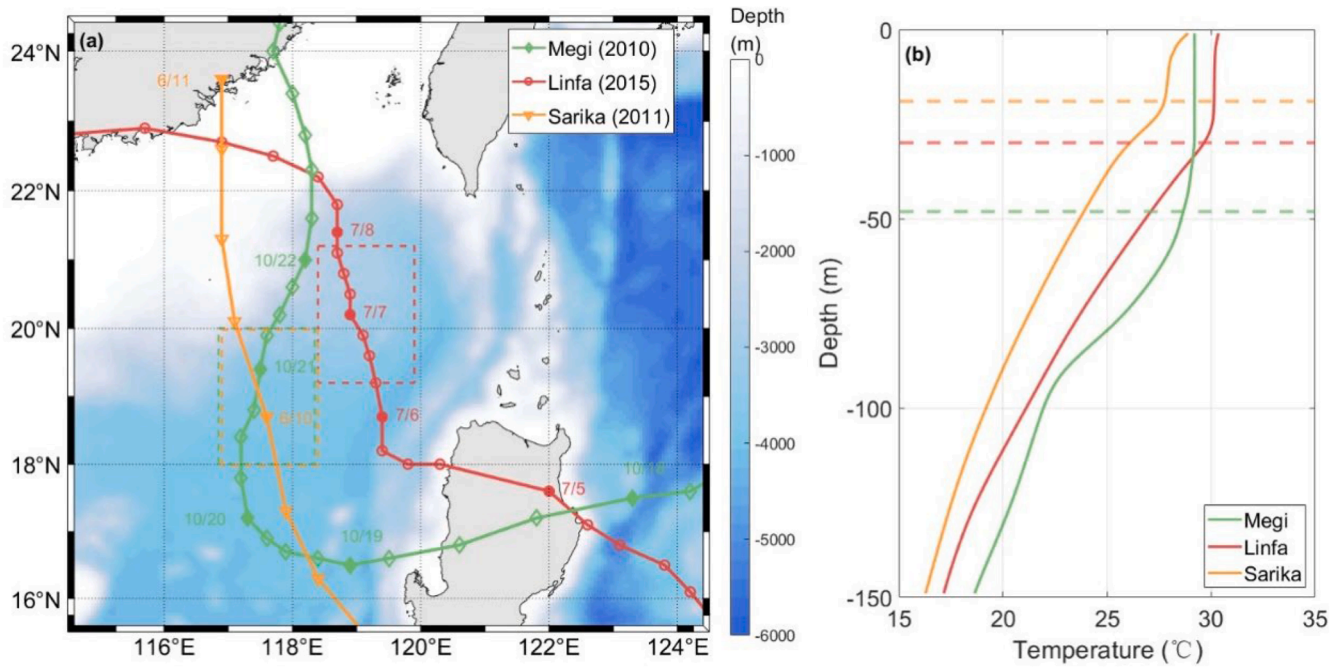
Fig. 1. (a) Bathymetry (shading, unit: m) of the northern SCS and tracks of Megi, Linfa, and Sarika (colored curves). The time is labeled every one day. The dashed boxes denote the study regions for the three typhoons. (b) Temperature profiles 2 days before the arrival of Megi, Linfa and Sarika, which are averaged in the dashed boxed in Fig. 1a. The dash lines represent the MLDs.

Table 1
Characteristics of Megi, Linfa, and Sarika from the best track dataset. The bold numbers represent typhoon's characteristics when its center was in the study region in Fig. 1a.

Typhoon characteristics	Typhoon	Time									
		−12h	−6h	0h	6h	12h	18h	24h	30h	36h	42h
Maximum wind speed (m/s)	Megi	50	50	**50**	**50**	**50**	**50**	50	50	50	45
	Linfa	23	20	**20**	**23**	**23**	**23**	**25**	**28**	28	28
	Sarika	13	15	**18**	**20**	**20**	18	18	18		
Pressure (hPa)	Megi	940	940	**940**	**940**	**940**	**940**	940	940	940	950
	Linfa	992	995	**995**	**992**	**992**	**992**	**990**	**985**	985	985
	Sarika	1002	1000	**998**	**995**	**995**	995	995	996		
Translation speed (m/s)	Megi	1.80	2.14	**3.13**	**3.09**	**2.28**	**3.13**	2.62	1.82	2.27	2.27
	Linfa	2.57	2.62	**2.12**	**1.62**	**1.82**	**1.54**	**1.62**	**1.62**	1.54	2.06
	Sarika	4.67	5.55	**6.53**	**7.48**	**6.93**	6.47	5.92	5.15		

interval are explored.

3. Methods

3.1. SSTC

The typhoon-induced SSTC was calculated as the difference between the minimum SST within 4 days after the typhoon and the SST 2 days before the typhoon. We calculated the SSTC induced by the three typhoons using remote sensing, CROCO simulations, and HYCOM reanalysis data. As shown in Fig. 1a, typhoons Megi and Sarika had turning stages in the SCS Basin. Considering that the turning stage of a typhoon (Li et al., 2020b; Zhang et al., 2023) and bathymetry (Pun et al., 2023) can influence the typhoon-induced SSTC, we chose three rectangular regions (1.5° longitude × 2° latitude) with depths greater than 1000 m, which were close to the typhoon tracks but away from the turning stages of Megi and Sarika, to study the SSTC induced by the three typhoons. The study region was 116.85–118.35° E, 18.00–20.00° N for Megi, 118.40–119.90° E, 19.20–21.20° N for Linfa, and 116.90–118.40° E, 18.00–20.00° N for Sarika, as indicated by the dashed boxes in Fig. 1a. For all three study regions, the area to the right of the typhoon track was almost 1.5 times larger than that to the left. Fig. 1b shows the vertical

temperature profiles averaged over the study regions two days before the arrival of the three typhoons. As shown, the water in June (October) had the largest (smallest) vertical temperature gradient and the shallowest (deepest) MLD before Sarika (Megi).

3.2. Temperature budget in the mixed layer

According to the temperature budget in the mixed layer (Jullien et al., 2012), we can investigate the SST variation during a typhoon as follows:

$$\frac{\partial SST}{\partial t} = -\frac{1}{h}\int_{-h}^{0}\left(u\frac{\partial T}{\partial x} + v\frac{\partial T}{\partial y}\right)dz - \frac{1}{h}\int_{-h}^{0}w\frac{\partial T}{\partial z}dz + \frac{1}{h}\int_{-h}^{0}K_l\left(\frac{\partial^2 T}{\partial x^2} + \frac{\partial^2 T}{\partial y^2}\right)dz$$
$$+ \left[-K_z\frac{1}{h}\frac{\partial T}{\partial z}(z=-h) - \frac{SST - T(z=-h)}{h}\frac{\partial h}{\partial t}\right] + \frac{Q}{\rho C_p h}$$

(1)

where T is the temperature, t is the time, x and y are zonal and meridional coordinates, z is the depth, u, v, and w are the zonal, meridional, and vertical velocities, respectively. K_l and K_z are the horizontal and vertical mixing coefficients, respectively, which depend on the shear. For K_z, the vertical shear is mainly caused by NIWs during the typhoon.

Q is the net heat flux, ρ is the density, C_p is the specific heat capacity, and h is the time-varying MLD. In this study, the MLD was calculated as the depth at which the temperature was 0.5 °C smaller than the temperature at 5 m depth (Sprintall & Tomczak, 1992; Watanabe & Hibiya, 2002; Cheng et al., 2023). The five terms on the right-hand side of Eq. (1) represent the horizontal advection (Hadv), vertical advection (Vadv), horizontal mixing (Hmix), vertical mixing (Vmix), and heat flux, respectively.

3.3. Wind power input (WPI)

The WPI to near-inertial motions is an important source of near-inertial energy in the ocean, and is calculated as follows (Dippe et al., 2015; Raja et al., 2022; Cao et al., 2023):

$$WPI = \tau \cdot u_f(z=0) \tag{2}$$

where τ is the near-inertial wind stress vector, and $\mathbf{u_f}$ is the near-inertial velocity vector. In this study, $\mathbf{u_f}$ and τ were obtained by bandpass filtering the raw velocity and wind stress with a cutoff frequency of [0.8, 1.2]f, where f is the local Coriolis frequency.

Fig. 2 shows the WPI of Megi, Linfa, and Sarika. The averaged WPI of Megi, Linfa and Sarika from the entry of the typhoon's center into the study region to 24 h after the typhoon's center left the study region was 3.53×10^{-1}, 3.01×10^{-2}, and 3.69×10^{-3} W/m^2, respectively. The averaged WPI of Linfa (Sarika) was one (two) order(s) of magnitude lower than that of Megi, which is generally consistent with their intensity (Table 1).

3.4. Modal decomposition of NIWs

Modal content is an important characteristic of NIWs. The modal decomposition method was used to extract the first M baroclinic modes of typhoon-induced NIWs (Zhao et al., 2010; Cao et al., 2023):

$$\begin{cases} u_f(z,t) = \sum_{m=0}^{M} u_{fm}(z,t) = \sum_{m=0}^{M} \widehat{u}_{fm}(t) \prod_m(z) \\ v_f(z,t) = \sum_{m=0}^{M} v_{fm}(z,t) = \sum_{m=0}^{M} \widehat{v}_{fm}(t) \prod_m(z) \end{cases} \tag{3}$$

where z is the depth, t is the time, u_f and v_f are the zonal and meridional near-inertial velocities, respectively, u_{fm} and v_{fm} are zonal and meridional near-inertial velocities, respectively, for the m-th mode (m=0 denotes the barotropic mode and m>0 the baroclinic modes), $\widehat{u}_{fm}$ and $\widehat{v}_{fm}$ are corresponding modal amplitudes of u_{fm} and v_{fm}, and Π_m is vertical structure function for the m-th mode, which is calculated as follows:

$$\prod_m(z) = \rho_0 c_m^2 \frac{d\Phi_m(z)}{dz} \tag{4}$$

$$\frac{d^2\Phi_m}{dz^2} + \frac{N^2}{c_m}\Phi_m = 0 \tag{5}$$

in which ρ_0 is the reference density, c_m is the eigenspeed, and N is buoyancy frequency. At the sea surface and bottom, $\Phi_m(0) = \Phi_m(-H) = 0$. Subsequently, the kinetic energy and shear for the modal NIWs were calculated.

4. Results

4.1. Typhoon-induced SSTC

Fig. 3 shows the SSTC induced by the three typhoons for the remote sensing data, CROCO simulations, and HYCOM reanalysis dataset. Table 2 lists the SSTC averaged in the study regions for the three typhoons. Remote sensing observations (Figs. 3a, e, and i) indicate that Megi and Sarika induced the largest and smallest SSTC, respectively. The SSTC induced by Linfa was intermediate between those induced by Megi and Sarika. For all three typhoons, the SSTC to the right side of the typhoon track was more considerable than that to the left side, which is consistent with the rightward biased feature of the ocean response to typhoons in the Northern Hemisphere (Price et al., 1994).

CROCO and HYCOM reproduced the SSTC induced by the three typhoons (Fig. 3b, c, f, g, j, and k), but CROCO performed better than HYCOM. The CROCO-simulated SSTC for the three typhoons was closer to the remote sensing observations than the SSTC obtained from the HYCOM dataset, and the root-mean-square errors (RMSEs) for the SSTC derived from CROCO simulations were smaller than those derived from the HYCOM dataset (Table 2). Fig. 3d, h, and l show point-to-point SSTC comparisons between the CROCO simulations (HYCOM dataset) and
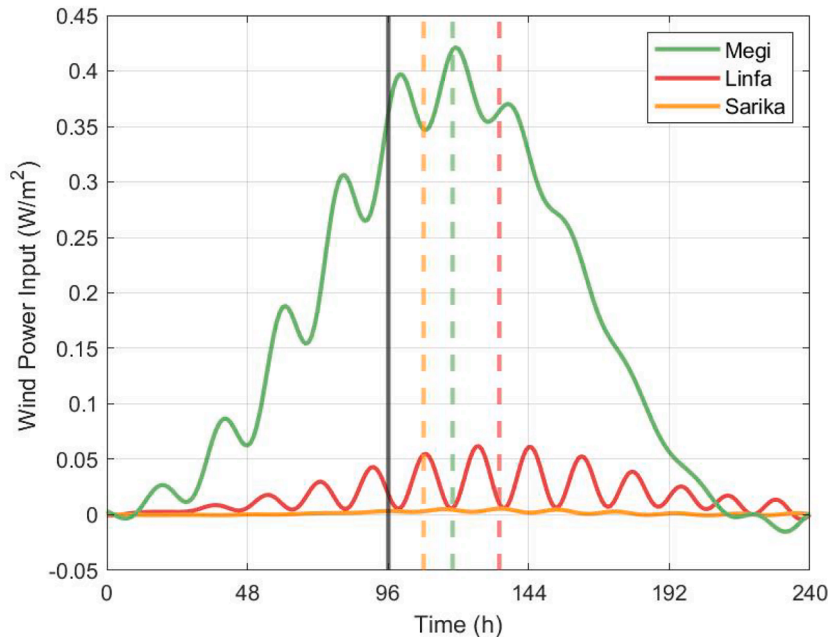

Fig. 2. WPI of Megi, Linfa, and Sarika. The solid (dashed) black (colored) lines indicate the time when the typhoons' center entered (left) the study region.
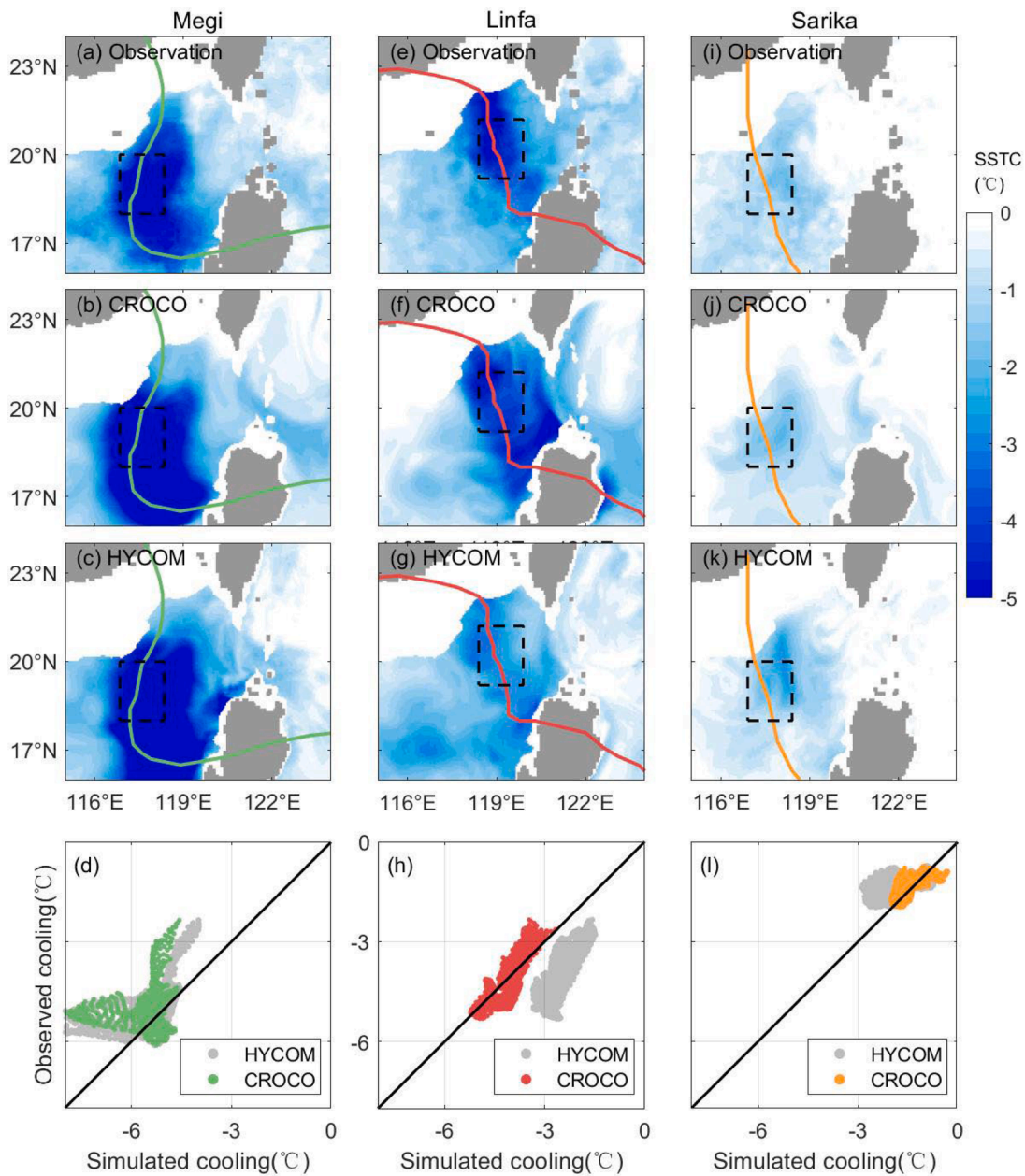
Fig. 3. SSTC (shading, unit: °C) derived from (a, e, i) remote sensing observations, (b, f, j) CROCO simulations, and (c, g, k) HYCOM reanalysis dataset caused by typhoons (a–c) Megi, (e–g) Linfa and (i–k) Sarika. Comparison of SSTC between CROCO model (HYCOM dataset) and remote sensing observation for typhoons (d) Linfa, (h) Sarika, and (l) Megi in the dashed boxes.

Table 2
SSTC induced by Megi, Linfa, and Sarika.

	Remote sensing	CROCO (RMSEs)	HYCOM (RMSEs)
Megi	5.09 °C	5.50 °C (0.89 °C)	6.21 °C (1.74 °C)
Linfa	4.12 °C	4.03 °C (0.45 °C)	2.58 °C (1.60 °C)
Sarika	1.32 °C	1.46 °C (0.32 °C)	1.69 °C (0.57 °C)

remote sensing observations for the three typhoons in the study regions to demonstrate this further. Remote sensing observations and HYCOM dataset were interpolated on CROCO grids for comparison. The CROCO simulations were evidently closer to the remote sensing observations. These comparisons suggest that CROCO performed better than HYCOM in simulating the SSTC induced by the three typhoons. Therefore,

CROCO simulations were used for analysis in the subsequent sections of this study.

Stronger typhoons usually induce larger SSTC than weaker typhoons. Therefore, it is reasonable to conclude that Megi and Sarika induced the largest and smallest SSTCs, respectively. However, notably, the SSTC induced by Linfa was nearly comparable to that induced by Megi (Table 2), although Linfa was much weaker than Megi (Table 1), and Linfa's WPI was also much smaller than that of Megi (Fig. 2). In the following section, we compare Linfa and Megi and explore why Linfa caused such a strong SSTC.

4.2. Temperature budget

The temperature budgets in the mixed layer were calculated to understand the cooling process in Megi and Linfa, as shown in Fig. 4. The derivative of SST was substantial from 48 to 192 h, which is consistent
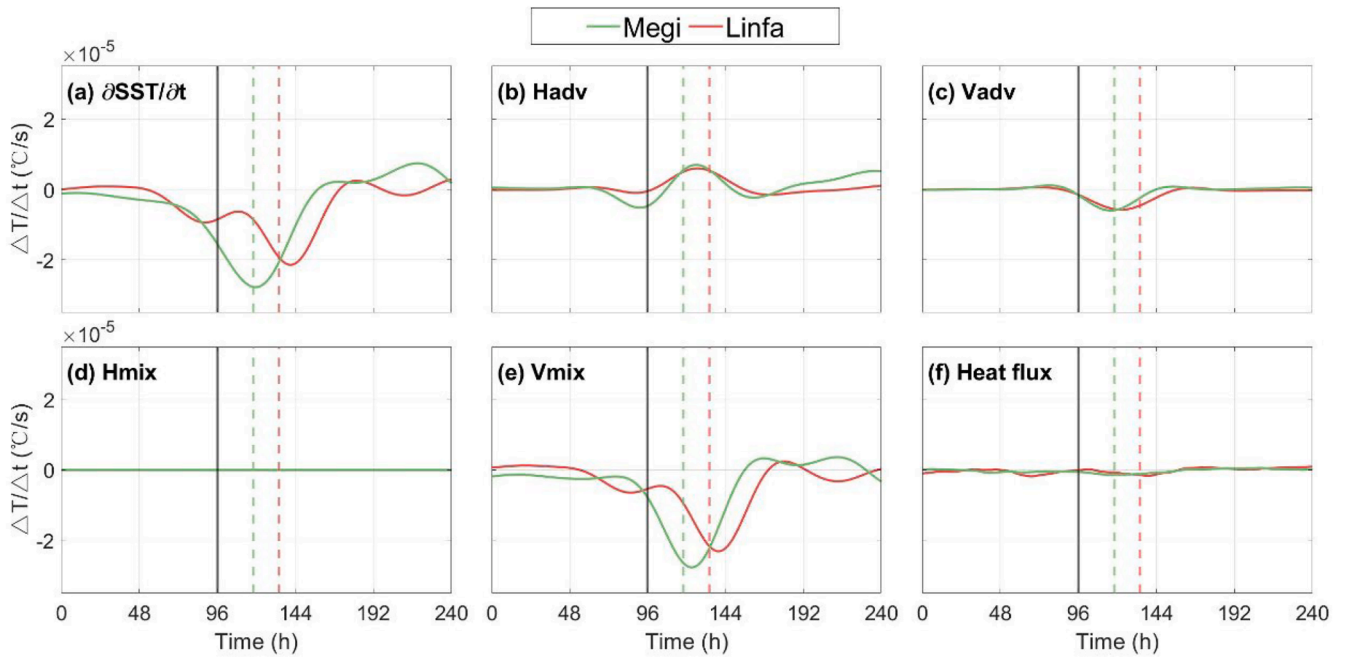
Fig. 4. (a) Derivative of SST with respect to time and the contributions of (b) Hadv, (c) Vadv, (d) Hmix, (e) Vmix, and (f) heat flux for typhoons Megi (green) and Linfa (red) averaged in the study regions. The solid (dashed) black (colored) lines indicate the time when the typhoons' center entered (left) the study region.

with the period that we used to calculate SSTC. For Megi and Linfa, the contributions of Hmix (Fig. 4d) and heat flux (Fig. 4f) to the SSTC were negligible. Therefore, the SSTC was mainly governed by the Vmix, Vadv, and Hadv (Fig. 4b, c, and e), which is consistent with previous studies (Price, 1981; Chiang et al., 2011; Emanuel, 2003; Jullien et al., 2012; Cheng et al., 2023). The Vmix and Vadv enhanced the SSTC by transporting the cold water to the upper ocean, whereas the Hadv suppressed the SSTC by bringing warm water away from the typhoon track to the study region. Among them, Linfa had even larger values of Vadv than Megi (Fig. 4c), which was associated with its larger vertical temperature

gradient (Fig. 1b) and slower translation speed. This contributed to the strong SSTC induced by Linfa but was not the main cause. Vmix contributed the most to SSTC for both Megi and Linfa. The comparable Vmix between Linfa and Megi yielded the strong SSTC induced by Linfa.

4.3. Vertical mixing

According to Eq. (1), Vmix is determined by the vertical temperature gradient ($\partial T/\partial z$), vertical mixing coefficient (Kz), the MLD (h), and its variation ($\partial h/\partial t$):
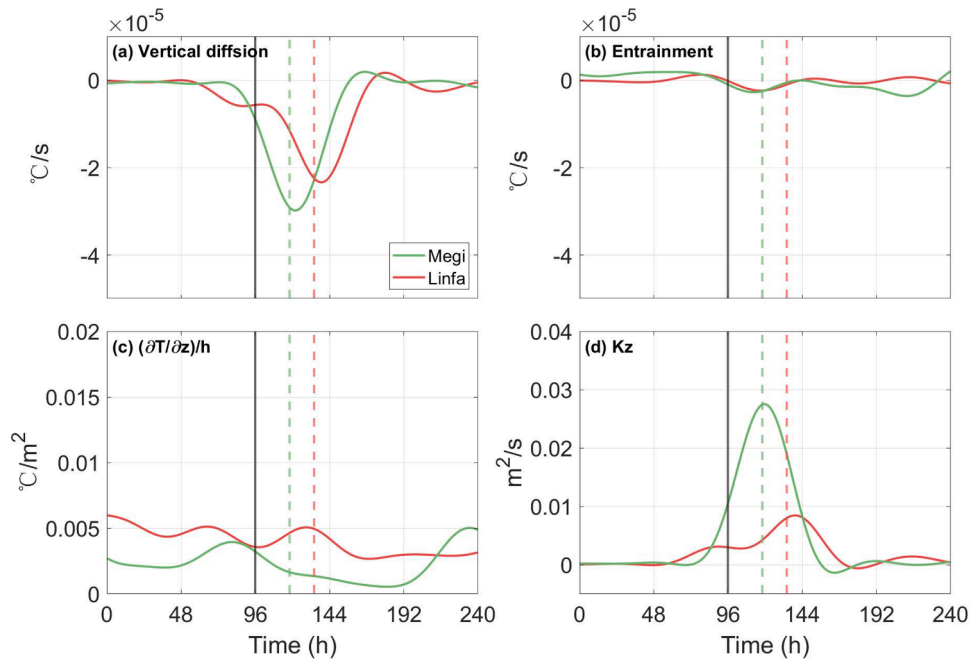

Fig. 5. (a) Vertical diffusion at the MLD, (b) entrainment, (c) temperature gradient divided by the MLD and (d) vertical mixing coefficient at the MLD for typhoons Megi (green) and Linfa (red) averaged in the study regions. The solid (dashed) black (colored) lines indicate the time when the typhoons' center entered (left) the study region.

$$V\text{mix} = -K_z\frac{1}{h}\frac{\partial T}{\partial z}(z = -h) - \frac{SST - T(z = -h)}{h}\frac{\partial h}{\partial t} \qquad (6)$$

The first term on the right hand side of Eq. (6) is vertical diffusion at the MLD, and the second term is entrainment (Vincent et al., 2012a; Jullien et al., 2012).

Fig. 5a and b show the vertical diffusion at the MLD and entrainment averaged in the study regions for Megi and Linfa. The vertical diffusion at the MLD was much larger than the entrainment, suggesting that the vertical diffusion at the MLD was dominant in Vmix, which is consistent with the result of idealized numerical simulation (Cheng et al., 2023).

Fig. 5c and d show the temperature gradient divided by the MLD [$(dT/dz)/h$] and the vertical mixing coefficient (K_z) at the MLD, both of which influence the vertical diffusion at the MLD (Eq. (6)). As shown in Fig. 5a, the vertical diffusion at the MLD for Megi and Linfa began to increase two days before the typhoon's center entered the study region (black vertical lines) and reached its maximum slightly after the typhoon's center left the study region (dashed vertical lines), and decreased to approximately zero four days after the typhoon's center entered the study region. Consequently, the period 48–192 h was selected to calculate the time-averaged values of $(dT/dz)/h$ and K_z. During this period, the mean $(dT/dz)/h$ of Megi and Linfa were 2.31×10^{-3} and 4.49×10^{-3} °C/m^2, respectively. The mean K_z values of Megi and Linfa were 7.71×10^{-3} and 2.85×10^{-3} m^2/s, respectively. Although both the mean K_z values of Megi and Linfa were on the order of 10^{-3} m^2/s, the former was nearly 3 times larger than the latter.

These results show that a combination of a relatively strong K_z and $(dT/dz)/h$ at the MLD results in a strong Vmix during Linfa, finally leading to a strong SSTC. The strong $(dT/dz)/h$ during Linfa was associated with the ocean background stratification (Fig. 1b): the SCS in July (Linfa occurrence) had a shallower MLD and higher SST than that in October (Megi occurrence), leading to higher $(dT/dz)/h$ (Vincent et al., 2012b; Wang et al., 2016; Guan et al., 2021). The mean K_z during Linfa was nearly one third of that during Megi, which cannot be easily

explained by the WPI to the ocean, as Linfa's WPI was one order of magnitude smaller than Megi's WPI (Fig. 2). Therefore, studying why weak typhoon Linfa caused a relatively significant vertical mixing coefficient, which reached one third of that during super typhoon Megi, is important.

4.4. Shear of NIWs

Fig. 6a and b show the power spectral densities (PSDs) of the zonal velocity (u) and zonal velocity vertical shear (du/dz) averaged over the upper 1000 m for Megi and Linfa, which were calculated based on CROCO simulations. A 15-day time series beginning five days before the typhoon's center entered the study region was used to calculate the PSDs. Therefore, the resolution of these spectra was 0.0067 cpd. The near-inertial peak was significant in the velocity spectra, with a value comparable to or slightly smaller than those of the diurnal and semi-diurnal internal tides. In the shear spectra, near-inertial signals dominated diurnal and semidiurnal internal tides. These results are generally consistent with previous observations in the SCS and demonstrate that during a typhoon event, the main driver of intense vertical shear is typhoon-induced NIWs (Jaimes and Shay, 2010; Xu et al., 2013; Hou et al., 2019; Cao et al., 2018; Cao et al., 2019).

Consistent with the intensity of the typhoons, Megi induced much stronger NIWs than Linfa, which were easily detected by near-inertial peak values in the velocity spectra. However, the near-inertial peak values in the shear spectra for Linfa and Megi were comparable, except that the former had a narrow peak, whereas the latter had a wide peak. Specifically, Linfa induced near-inertial shear comparable to that of Megi, although Linfa induced weaker NIWs. This result is further confirmed by the near-inertial kinetic energy and shear squared (Fig. 6c and d). The maximum kinetic energy appeared near the surface, whereas the shear squared reached its maximum at the MLD, explaining the occurrence of strong vertical diffusion at the MLD (Fig. 5a). The near-
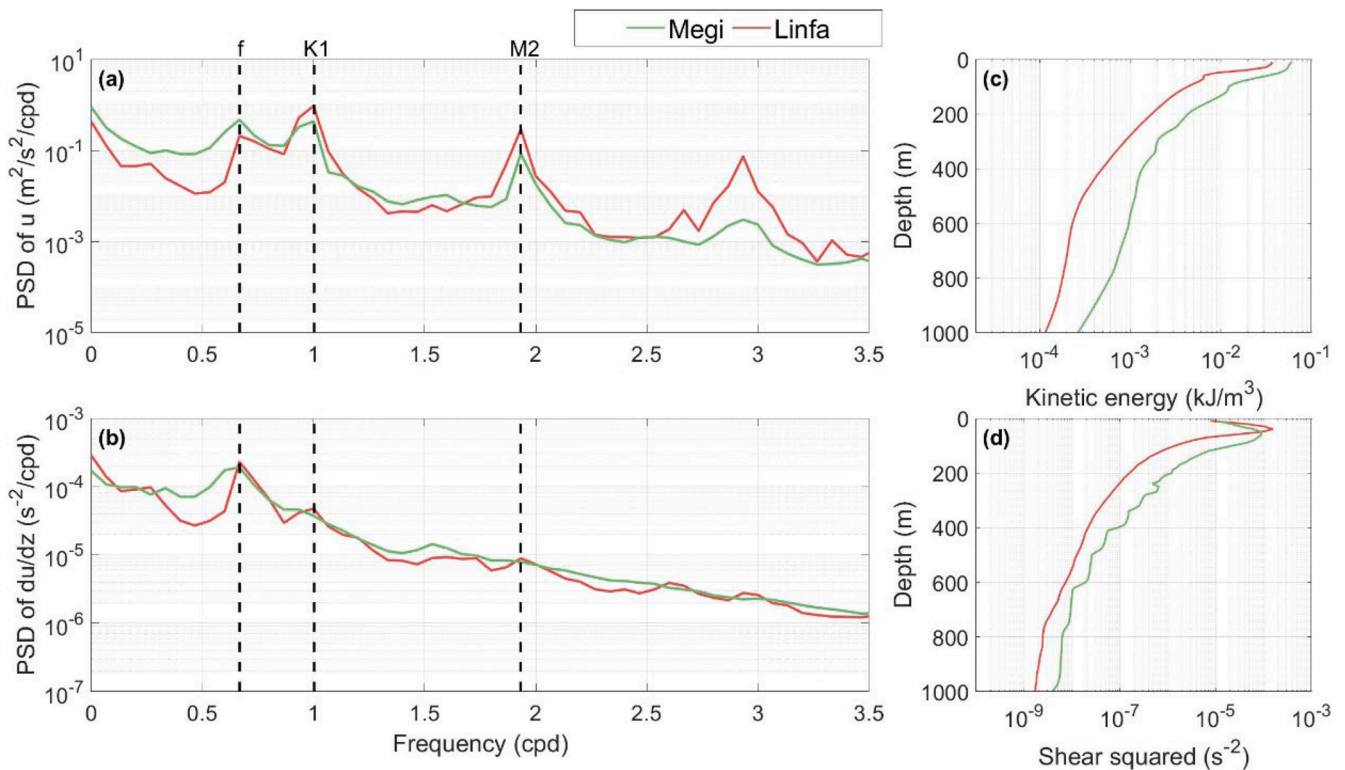

Fig. 6. PSDs of (a) zonal velocity (b) zonal velocity vertical shear averaged in the upper 1000 m for Megi and Linfa. Vertical distributions of (c) kinetic energy and (d) shear squared of near-inertial waves induced by Megi and Linfa.
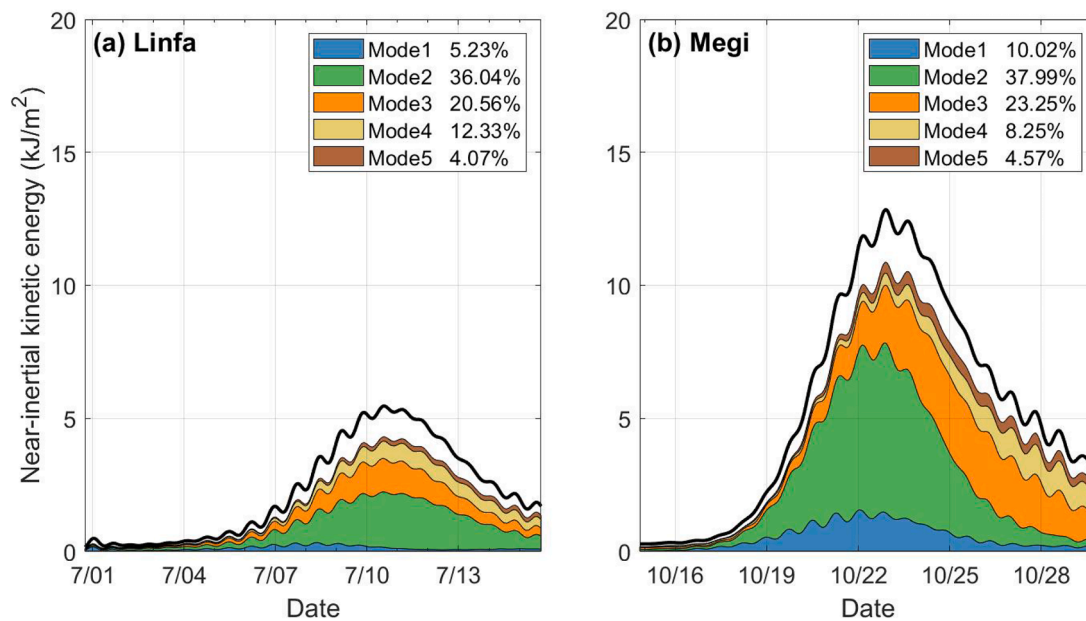
Fig. 7. Depth-integrated near-inertial kinetic energy of (a) Linfa and (b) Megi in each baroclinic mode. In each subfigure, the black solid curve denotes the total near-inertial kinetic energy.

inertial kinetic energy induced by Linfa was smaller than that induced by Megi at all depths (Fig. 6c), however, the near-inertial shear squared induced by Linfa at the MLD was even stronger than that induced by Megi (Fig. 6d).

4.5. Modal content of NIWs

To understand why the weaker NIWs induced by Linfa caused comparable shear to the stronger NIWs induced by Megi, attention was focused on the modal content of the NIWs. Fig. 7a and b show the near-inertial kinetic energy of the first five baroclinic modes and their proportions of the total near-inertial kinetic energy for Linfa and Megi, respectively. Linfa- and Megi-induced NIWs were dominated by mode-2, followed by mode-3, but their proportions differed. The proportions of mode-1 to mode-3 in the total near-inertial kinetic energy for the Megi-induced NIWs were 10.02 %, 37.99 %, and 23.25 %, respectively, all of which were larger than those for the Linfa-induced NIWs (5.23 %, 36.04 %, and 20.56 %, respectively). Therefore, mode-4, mode-5, and higher modes accounted for a smaller proportion of Megi-induced NIWs (28.74 %) than Linfa-induced NIWs (38.17 %).

NIWs characterized by high-mode features have large vertical wavenumbers and small vertical wavelengths; thus, they considerably contribute to upper ocean vertical shear (Jaimes & Shay, 2010; Alford et al., 2016; Hou et al., 2019). To demonstrate this, the vertical shear for each mode was calculated separately (Fig. 8). Note that the vertical shear does not satisfy linear superposition. Hence, the sum of vertical shear in each mode was not equal to the total shear. Fig. 8 evidently shows that mode-4, mode-5, and higher-mode NIWs induced by Linfa contributed more to the total vertical shear than those induced by Megi. This result explains why the weaker NIWs induced by Linfa caused a comparable vertical shear as the stronger NIWs induced by Megi (Fig. 6).

5. Discussion

Typhoon characteristics, including the maximum wind speed, radius

of the maximum wind speed and translation speed, and ocean background conditions, such as ocean stratification, sea level anomalies, SST and MLD, can influence typhoon-induced SSTC (e.g. Lin et al., 2008; 2009; Vincent et al., 2012a; 2012b). Considering the contributions of these factors, the SSTC induced by many typhoons can be predicted (Vincent et al., 2012b; Cui et al., 2023). However, there are still some typhoons that induced stronger SSTC than expected.

This study shows that the influences of the above factors on SSTC are different for different typhoon cases, which allows a weak typhoon with a maximum wind speed below 30 m/s to induce a large SSTC. Linfa caused a SSTC almost comparable to that of the super typhoon Megi under a combination of a relatively strong vertical mixing coefficient and vertical temperature gradient (Figs. 4 and 5). The strong vertical temperature gradient during Linfa was caused by ocean stratification in July (Fig. 1b), as shallower MLD and higher SST enhance temperature gradient at the MLD (Vincent et al., 2012b). Moreover, the relatively high mixing coefficient was also associated with ocean stratification which influenced the characteristics of typhoon-induced NIWs (e.g., Cao et al., 2023). The WPI of Linfa was an order of magnitude smaller than that of Megi (Fig. 2), and Linfa-induced NIWs were weaker than Megi-induced NIWs (Fig. 6). However, the differences in stratification during these two typhoons resulted in elevated proportions of mode-4, mode-5, and higher modes in Linfa-induced NIWs compared to those in Megi-induced NIWs (Fig. 7), which contributed more to the total vertical shear in the upper ocean (Fig. 8). As a result, the vertical mixing coefficient during Linfa reached one third of that during Megi, and the SSTC induced by Linfa was almost comparable to that induced by Megi. These results highlight the contribution of high-mode NIWs to enhanced typhoon-induced SSTC in the deep water.

This situation is different in the shallow water. Yang et al. (2015) studied the ocean dynamical and thermal responses to three typhoons (Washi, Vicente and Damrey in 2005) in the shallow water of the northwestern SCS. They found that typhoon Damrey induced the largest subsurface temperature cooling of 4.5 °C at the mooring, although Damrey-induced NIWs are dominated by the barotropic mode (mode-0).
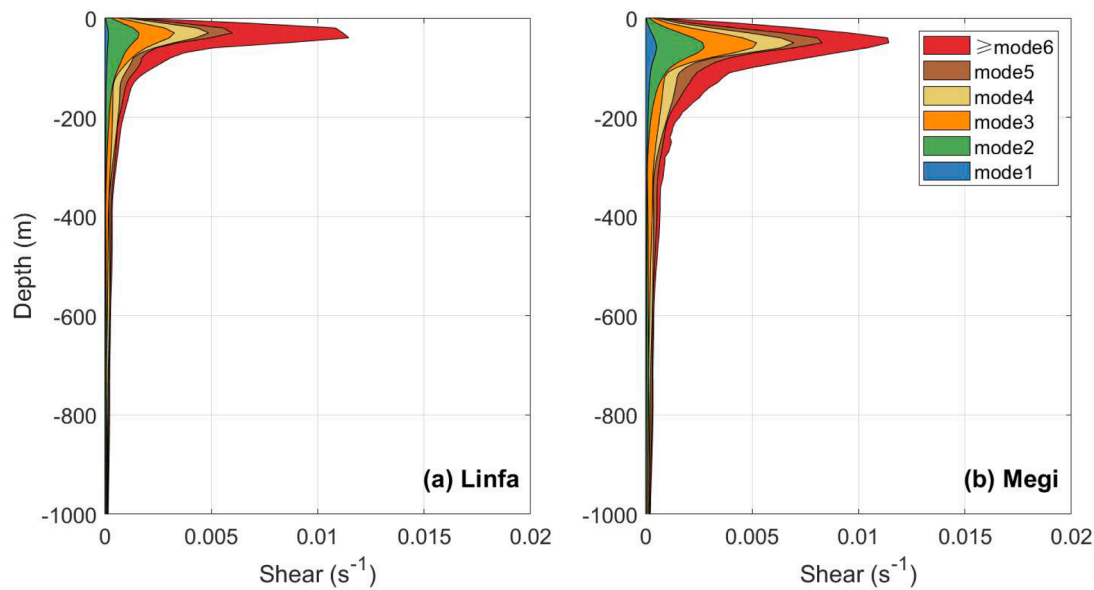
Fig. 8. Vertical shear caused by (a) Linfa and (b) Megi in each baroclinic mode.

In contrast, Washi-induced NIWs were dominated by the first baroclinic mode (mode-1), but the subsurface temperature cooling induced by Washi was only 2 °C. These conclusions are different from those in the deep water in this study, but they can be explained. According to Cao et al. (2023), the dominant modes of NIWs in shallow and deep waters are different. The NIWs are usually dominated by low mode in the shallow water but by high modes in the deep water. Hence, in the shallow water, the wind of typhoon rather than typhoon-induced NIWs is the main driver of turbulent mixing, whereas in the deep water, typhoon-induced high-mode NIWs have a considerable contribution to the enhanced turbulent mixing. Considering that Damrey is the strongest among the three typhoons (Washi, Vicente and Damrey), it is reasonable that Damrey induced the largest subsurface temperature cooling at the mooring. In addition, the simulated results of Rayson et al. (2015) on the Australian North-West Shelf also indicate that typhoons can damage the stratification in the shallow water, which is another evidence for the wind of typhoon rather than typhoon-induced NIWs being the main driver of turbulent mixing in the shallow water.

According to previous studies, the modal content of typhoon-induced NIWs could be different in different typhoon cases and show spatial dependence (e.g. Shay & Chang, 1997; Shay et al., 1998; Yang et al., 2015; He et al., 2022; Cao et al., 2023), which may have different contributions to the typhoon-induced SSTC. Therefore, the modal content of typhoon-induced NIWs should be properly considered in the development of typhoon-induced SSTC prediction model in the future.

6. Conclusion

This study investigated the SSTC induced by typhoons Megi (October 2010), Linfa (July 2015), and Sarika (June 2011), which traversed the SCS basin from south to north, following relatively similar tracks. Among the three typhoons, Megi was the strongest, Linfa was the moderate and Sarika was the weakest. In the study regions, the averaged SSTC induced by Megi, Linfa, and Sarika were 5.09 °C, 4.12 °C, and 1.32 °C, respectively. Notably, weak typhoon Linfa caused the SSTC almost comparable to that of super typhoon Megi.

The analysis of temperature budgets showed that vertical mixing, vertical advection, and horizontal advection control typhoon-induced SSTC. Vertical mixing and advection enhance the SSTC, whereas horizontal advection weakens it. Vertical mixing was the largest and dominated the SSTC. Further analysis showed that vertical mixing was dominated by vertical diffusion at the MLD, which was associated with the temperature gradient divided by the MLD and the vertical mixing coefficient at the MLD. Although Linfa was much weaker than Megi, the vertical diffusion at the MLD during Linfa was comparable to that during Megi because of the relatively strong vertical mixing coefficient and vertical temperature gradient, which was attributed to stratification differences during the two typhoons. First, stratification differences caused the temperature gradient divided by the MLD during Linfa to be larger than that during Megi. Second, although Linfa-induced NIWs were weaker than Megi-induced NIWs because the WPI during Linfa was an order of magnitude smaller than that during Megi, the stratification differences led to Linfa-induced NIWs having larger proportions of mode-4, mode-5, and higher modes than Megi-induced NIWs. Consequently, the vertical mixing coefficient in the MLD during Linfa reached one third of that during Megi.

Although this study only focused on three typhoon cases with relatively similar tracks, the mechanisms underlying SSTC can be extrapolated more broadly. In addition, we only focused on the SSTC induced by typhoons, the effect of the ocean feedback on typhoons was not considered. It will be investigated in future studies by an air-sea coupled numerical simulation, which can further deepen our understanding of air-sea interaction and typhoon prediction.

CRediT authorship contribution statement

Shukui Cheng: Writing – original draft, Visualization, Software, Methodology, Formal analysis. **Anzhou Cao:** Writing – review & editing, Writing – original draft, Funding acquisition, Conceptualization. **Jinbao Song:** Writing – review & editing, Supervision. **Xinyu Guo:** Writing – review & editing, Supervision.

Declaration of competing interest

The authors declare that they have no known competing financial interests or personal relationships that could have appeared to influence the work reported in this paper.

Acknowledgments

Appendix A. Influence of model resolution

Results of numerical simulation are sensitive to the model resolution. To validate that the 1/20° resolution used in this study is sufficient to investigate typhoon-induced SSTC, we conducted two sensitivity simulations for Linfa by using model resolution of 1/10° and 1/30° As shown in Fig. A1, the SSTC and Vmix were a little weaker with a coarse resolution (1/10°). However, when the model resolution increases from 1/20° to 1/30°, the temperature budget was nearly the same. These results suggest that the 1/20° resolution used in this study is sufficient to investigate typhoon-induced SSTC.
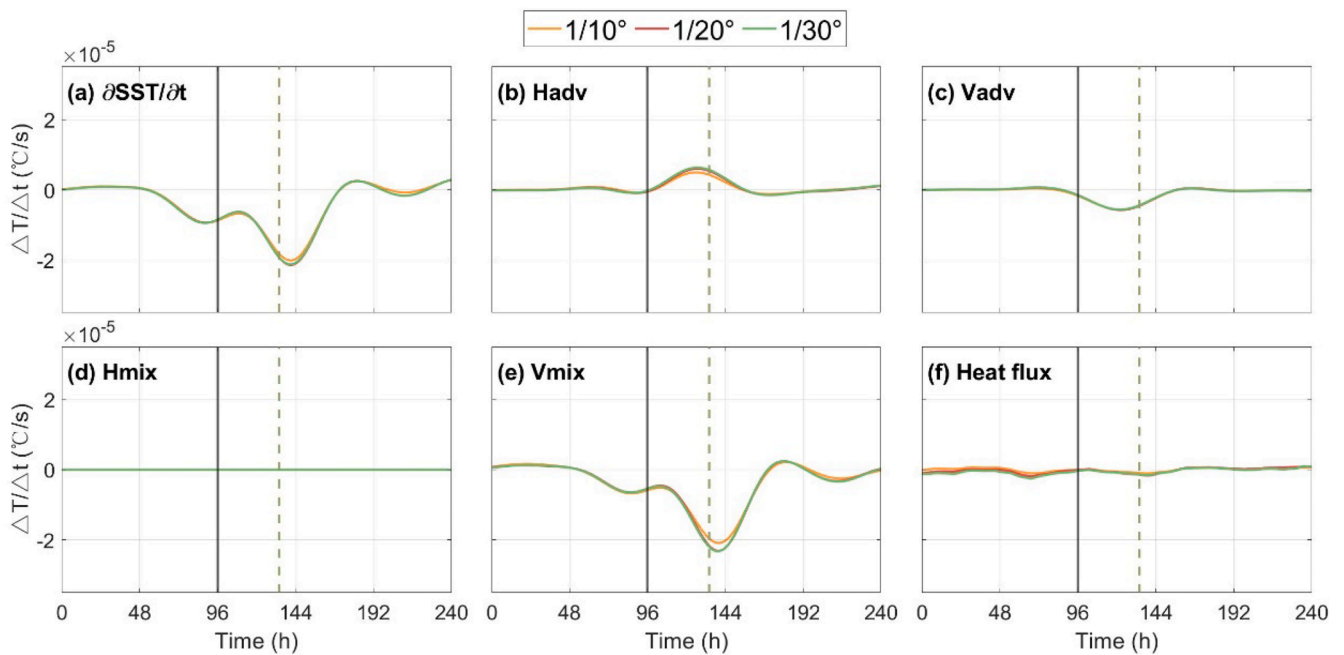

Fig. A1. Same as Fig. 4 for Linfa but for different model resolution.

Appendix B. Influence of vertical mixing scheme

In the numerical simulation, the vertical mixing was controlled by the vertical mixing scheme. In the KPP scheme, the vertical mixing coefficients of the oceanic surface boundary layer and the ocean interior were calculated separately. In addition to turbulent processes, surface forcing, such as wind stress, is also considered in the KPP scheme (Large et al., 1994). During typhoon events, the oceanic surface boundary layer and surface forcing vary significantly. Therefore, we conducted a sensitivity simulation for Linfa based on the Generic Length Scale (GLS) scheme (Jones & Launder, 1972), which does not distinguish the oceanic surface boundary layer and ocean interior and does not consider surface stress. A comparison of the temperature budgets during Linfa for the two runs based on the KPP and GLS schemes is shown in Fig. B1. The results based on the two different vertical mixing schemes were nearly the same, except for slight differences in the values of the derivative of SST, vertical mixing, and vertical advection. In other words, the choice of the vertical mixing scheme did not significantly change the temperature budget in the mixed layer.
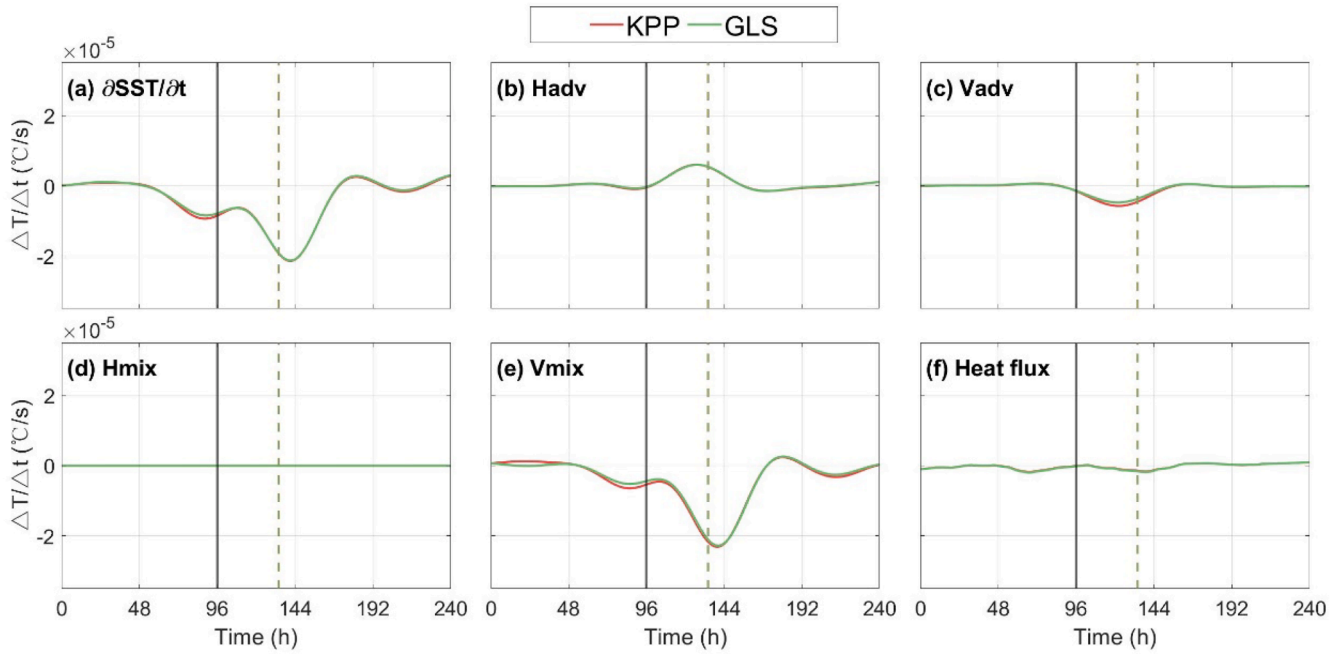
Fig. B1. Same as Fig. 4 for Linfa but for different vertical mixing schemes.

Appendix C. Influence of output interval

In the numerical simulations, the time step was 120 s, and the output interval was 1 h (3600 s). Therefore, the variation within 1 h was ignored, which may have led to a bias in the temperature budget analysis. Therefore, we conducted a sensitivity simulation for Linfa by outputting results every 120 s. A comparison of the temperature budgets during Linfa for the two output intervals is shown in Fig. C1. The results of the two different output intervals were nearly the same, suggesting that an output interval within 1 h did not significantly influence the temperature budget.
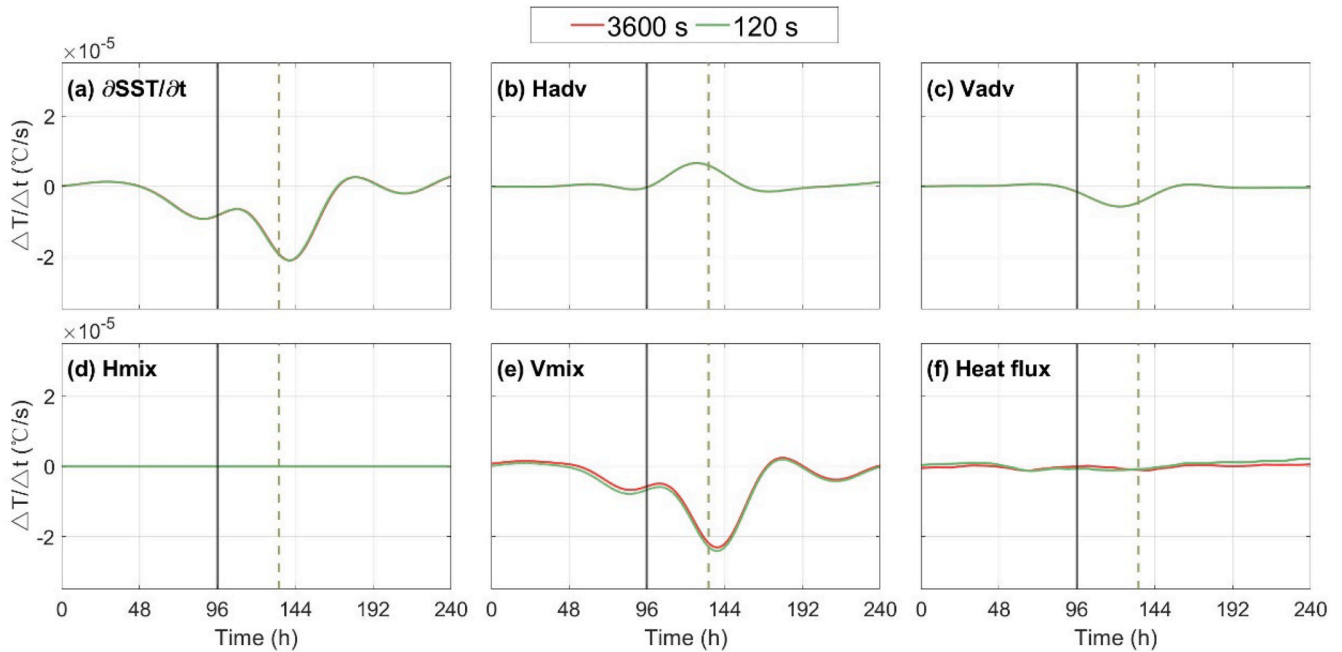

Fig. C1. Same as Fig. 4 for Linfa but for different output intervals.

Data availability

Data will be made available on request.

CROCO code and barotropic tidal forcing data are available at www.croco-ocean.org. The Tropical Cyclone best track data are available at http://tcdata.typhoon.org.cn. The CFSR surface forcing data and

ETOPO1 bathymetry data are available at apdrc.soest.hawaii. edu/data/data.php. The HYCOM Reanalysis data are available at https://www.hycom.org/. The remote sensing sea surface temperature data are available at https://www.remss.com/measurements /sea-surface-temperature/.

References

Alford, M.H., MacKinnon, J.A., Simmons, H.L., Nash, J.D., 2016. Near-inertial internal gravity waves in the ocean. Ann. Rev. Mar. Sci. 8, 95–123. https://doi.org/10.1146/annurev-marine-010814-015746 (Volume 8, 2016).

Balaguru, K., Chang, P., Saravanan, R., Leung, L.R., Xu, Z., Li, M., Hsieh, J., 2012. Ocean barrier layers' effect on tropical cyclone intensification. Proc. Natl. Acad. Sci. 109 (36), 14343–14347. https://doi.org/10.1073/pnas.1201364109.

Bender, M.A., Ginis, I., Kurihara, Y., 1993. Numerical simulations of tropical cyclone-ocean interaction with a high-resolution coupled model. J Geophys Res. Atmos. 98 (D12), 23245–23263. https://doi.org/10.1029/93JD02370.

Cao, A., Guo, Z., Song, J., Lv, X., He, H., Fan, W., 2018. Near-inertial waves and their underlying mechanisms based on the south china sea internal wave experiment (2010–2011). J. Geophys. Res. Oceans 123 (7), 5026–5040. https://doi.org/10.1029/2018JC013753.

Cao, A., Guo, Z., Wang, S., Chen, X., Lv, X., Song, J., 2019. Upper ocean shear in the northern South China Sea. J. Oceanogr. 75 (6), 525–539. https://doi.org/10.1007/s10872-019-00520-x.

Cao, A., Wang, S., Morimoto, A., Takikawa, T., Guo, X., 2023. Modal content of typhoon-induced near-inertial waves around the East China Sea. Cont. Shelf. Res. 264, 105055. https://doi.org/10.1016/j.csr.2023.105055.

Chan, J., 2005. Interannual and interdecadal variations of tropical cyclone activity over the Western North Pacific. Meteorol. Atmos. Phys. 89, 143–152. https://doi.org/10.1007/s00703-005-0126-y.

Cheng, S., Cao, A., He, H., Li, P., Song, J., 2023. Numerical study on the influence of internal tides on tropical-cyclone-induced sea surface temperature cooling in the South China Sea. Ocean Dyn. 73 (7), 449–461. https://doi.org/10.1007/s10236-023-01561-z.

Chiang, T., Wu, C., Oey, L., 2011. Typhoon Kai-Tak: an ocean's perfect storm. J. Phys. Oceanogr. 41 (1), 221–233. https://doi.org/10.1175/2010JPO4518.1.

Cui, H., Tang, D., Mei, W., Liu, H., Sui, Y., Gu, X., 2023. Predicting tropical cyclone-induced sea surface temperature responses using machine learning. Geophys. Res. Lett. 50 (18), e2023GL104171. https://doi.org/10.1029/2023GL104171.

Dare, R.A., McBride, J.L., 2011. Sea surface temperature response to tropical cyclones. Mon. Weather Rev. 139 (12), 3798–3808. https://doi.org/10.1175/MWR-D-10-05019.1.

Dippe, T., Zhai, X., Greatbatch, R.J., Rath, W., 2015. Interannual variability of wind power input to near-inertial motions in the North Atlantic. Ocean Dyn. 65 (6), 859–875. https://doi.org/10.1007/s10236-015-0834-x.

Egbert, G.D., Erofeeva, S.Y., 2002. Efficient inverse modeling of barotropic ocean tides. J. Atmos. Ocean. Technol. 19 (2), 183–204. https://doi.org/10.1175/1520-0426(2002)019<0183:EIMOBO>2.0.CO;2.

Emanuel, K., 2003. Tropical cyclones. Annu. Rev. Earth Planet. Sci. 31 (1), 75–104. https://doi.org/10.1146/annurev.earth.31.100901.141259.

Greatbatch, R.J., 1984. On the response of the ocean to a moving storm: parameters and scales. J. Phys. Oceanogr. 14 (1), 59–78. https://doi.org/10.1175/1520-0485(1984)014<0059:OTROTO>2.0.CO;2.

Guan, S., Zhao, W., Huthnance, J., Tian, J., Wang, J., 2014. Observed upper ocean response to typhoon Megi (2010) in the Northern South China Sea. J Geophys. Res. Oceans 119 (5), 3134–3157. https://doi.org/10.1002/2013JC009661.

Guan, S., Zhao, W., Sun, L., Zhou, C., Liu, Z., Hong, X., et al., 2021. Tropical cyclone-induced sea surface cooling over the Yellow Sea and Bohai Sea in the 2019 Pacific typhoon season. J. Mar. Syst. 217, 103509. https://doi.org/10.1016/j.jmarsys.2021.103509.

He, H., Cao, A., Wang, Y., Song, J., 2022. Evolution of oceanic near-inertial waves induced by typhoon Sarika (2016) in the South China Sea. Dyn. Atmos. Oceans 100, 101332. https://doi.org/10.1016/j.dynatmoce.2022.101332.

Hou, H., Yu, F., Nan, F., Yang, B., Guan, S., Zhang, Y., 2019. Observation of near-inertial oscillations induced by energy transformation during typhoons. Energies 12 (1), 99. https://doi.org/10.3390/en12010099. . (Basel).

Huang, P., Sanford, T., Imberger, J., 2009. Heat and turbulent kinetic energy budgets for surface layer cooling induced by the passage of hurricane Frances (2004). J. Geophys. Res. 114. https://doi.org/10.1029/2009JC005603.

Jacob, S., Shay, L., Mariano, A., Black, P., 2000. The 3D oceanic mixed layer response to hurricane gilbert. J. Phys. Oceanogr. 30, 1407–1429. https://doi.org/10.1175/1520-0485(2000)030<1407:TOMLRT>2.0.CO;2.

Jaimes, B., Shay, L., 2010. Near-inertial wave wake of hurricanes katrina and rita over mesoscale oceanic eddies. J. Phys. Oceanogr. 40, 1320–1337. https://doi.org/10.1175/2010JPO4309.1.

Jones, W.P., Launder, B., 1972. The prediction of laminarization with a two-equation model of turbulence. Int. J. Heat Mass Transf. 15, 301–314. https://doi.org/10.1016/0017-9310(72)90076-2.

Jullien, S., Menkes, C., Marchesiello, P., Jourdain, N., Lengaigne, M., Koch-Larrouy, A., et al., 2012. Impact of tropical cyclones on the heat budget of the south pacific ocean. J. Phys. Oceanogr. 42, 1882–1906. https://doi.org/10.1175/JPO-D-11-0133.1.

Ko, D.S., Chao, S., Wu, C., Lin, I., 2014. Impacts of typhoon megi (2010) on the South China Sea. J. Geophys. Res. Oceans 119 (7), 4474–4489. https://doi.org/10.1002/2013JC009785.

Krishnaja, P.B., Akhila, R.S., Kuttippurath, J., Sunanda, N., 2024. Tropical cyclone-driven rainfall in the northeast Indian Ocean and adjoining land regions during the period 2000–2020. J. Hydrol. 629, 130610. https://doi.org/10.1016/j.jhydrol.2024.130610.

Large, W.G., McWilliams, J.C., Doney, S.C., 1994. Oceanic vertical mixing: a review and a model with a nonlocal boundary layer parameterization. Rev. Geophys. 32 (4), 363–403. https://doi.org/10.1029/94RG01872.

Li, A., Guan, S., Mo, D., Hou, Y., Hong, X., Liu, Z., 2020a. Modeling wave effects on storm surge from different typhoon intensities and sizes in the South China Sea. Estuar. Coast. Shelf Sci. 235, 106551. https://doi.org/10.1016/j.ecss.2019.106551.

Li, J., Yang, Y., Wang, G., Cheng, H., Sun, L., 2020b. Enhanced oceanic environmental responses and feedbacks to super typhoon Nida (2009) during the sudden-turning stage. Remote Sens. 13, 2648. -Basel.

Lin, I., Pun, I., Wu, C., 2009. Upper-ocean thermal structure and the Western north pacific category 5 typhoons. Part II: dependence on translation speed. Mon. Weather Rev. 137 (11), 3744–3757. https://doi.org/10.1175/2009MWR2713.1.

Lin, I., Wu, C., Pun, I., Ko, D., 2008. Upper-ocean thermal structure and the Western North pacific category 5 typhoons. Part I: ocean features and the category 5 typhoons' intensification. Mon. Weather Rev. 136 (9), 3288–3306. https://doi.org/10.1175/2008MWR2277.1.

Liu, Y., Guan, S., Lin, I.I., Mei, W., Jin, F., Huang, M., et al., 2023. Effect of storm size on sea surface cooling and tropical cyclone intensification in the Western North Pacific. J. Clim. 36 (20), 7277–7296. https://doi.org/10.1175/JCLI-D-22-0949.1.

Lu, X., Yu, H., Ying, M., Zhao, B., Zhang, S., Lin, L., et al., 2021. Western North pacific tropical cyclone database created by the China meteorological administration. Adv. Atmos. Sci. 38 (4), 690–699. https://doi.org/10.1007/s00376-020-0211-7.

Neetu, S., Lengaigne, M., Vincent, E.M., Vialard, J., Madec, G., Samson, G., et al., 2012. Influence of upper-ocean stratification on tropical cyclone-induced surface cooling in the Bay of Bengal. J. Geophys. Res. Oceans 117 (C12). https://doi.org/10.1029/2012JC008433.

Pei, Y., Zhang, R., Chen, D., 2015. Upper ocean response to tropical cyclone wind forcing: a case study of typhoon Rammasun (2008). Sci. China Earth Sci. 58 (9), 1623–1632. https://doi.org/10.1007/s11430-015-5127-1.

Price, J.F., 1981. Upper ocean response to a hurricane. J. Phys. Oceanogr. 11 (2), 153–175. https://doi.org/10.1175/1520-0485(1981)011<0153:UORTAH>2.0.CO;2.

Price, J.F., Sanford, T.B., Forristall, G.Z., 1994. Forced stage response to a moving hurricane. J. Phys. Oceanogr. 24 (2), 233–260. https://doi.org/10.1175/1520-0485(1994)024<0233:FSRTAM>2.0.CO;2.

Pun, I., Hsu, H., Moon, I., Lin, I., Jeong, J., 2023. Marine heatwave as a supercharger for the strongest typhoon in the East China Sea. npj Clim. Atmos. Sci. 6 (1), 128. https://doi.org/10.1038/s41612-023-00449-5.

Pun, I., Lin, I.I., Lien, C., Wu, C., 2018. Influence of the size of supertyphoon Megi (2010) on SST cooling. Mon. Weather Rev. 146 (3), 661–677. https://doi.org/10.1175/MWR-D-17-0044.1.

Qiao, M., Cao, A., Song, J., Pan, Y., He, H., 2022. Enhanced turbulent mixing in the upper ocean induced by super typhoon goni (2015). Remote Sens. 14 (10), 2300. https://doi.org/10.3390/rs14102300. -Basel.

Raja, K.J., Buijsman, M.C., Shriver, J.F., Arbic, B.K., Siyanbola, O., 2022. Near-inertial wave energetics modulated by background flows in a global model simulation. J. Phys. Oceanogr. 52 (5), 823–840. https://doi.org/10.1175/JPO-D-21-0130.1.

Rayson, M.D., Ivey, G.N., Jones, N.L., Lowe, R.J., Wake, G.W., McConochie, J.D., 2015. Near-inertial ocean response to tropical cyclone forcing on the Australian North-West Shelf. J. Geophys. Res. Oceans 120 (12), 7722–7751. https://doi.org/10.1002/2015JC010868.

Schade, L.R., Emanuel, K.A., 1999. The ocean's effect on the intensity of tropical cyclones: results from a simple coupled atmosphere–ocean model. J. Atmos. Sci. 56 (4), 642–651. https://doi.org/10.1175/1520-0469(1999)056<0642:TOSEOT>2.0.CO;2.

Shay, L.K., Chang, S.W., Elsberry, R.L., 1990. Free surface effects on the near-inertial ocean current response to a hurricane. J. Phys. Oceanogr. 20 (9), 1405–1424. https://doi.org/10.1175/1520-0485(1990)020<1405:FSEOTN>2.0.CO;2.

Shay, L.K., Black, P.G., Mariano, A.J., Hawkins, J.D., Elsberry, R.L., 1992. Upper ocean response to hurricane gilbert. J Geophys. Res. Oceans 97 (C12), 20227–20248. https://doi.org/10.1029/92JC01586.

Shay, L.K., Chang, S.W., 1997. Free surface effects on the near-inertial ocean current response to a hurricane: a revisit. J. Phys. Oceanogr. 27 (1), 23–39. https://doi.org/10.1175/1520-0485(1997)027<0023:FSEOTN>2.0.CO;2.

Shay, L.K., Mariano, A.J., Jacob, S.D., Ryan, E.H., 1998. Mean and near-inertial ocean current response to hurricane gilbert. J. Phys. Oceanogr. 28 (5), 858–889. https://doi.org/10.1175/1520-0485(1998)028<0858:MANIOC>2.0.CO;2.

Shi, J., Feng, X., Toumi, R., Zhang, C., Hodges, K., Tao, A., Zhang, W., 2024. Global increase in tropical cyclone ocean surface waves. Nat. Commun. 15. https://doi.org/10.1038/s41467-023-43532-4.

Sprintall, J., Tomczak, M., 1992. Evidence of the barrier layer in the surface layer of the tropics. J. Geophys. Res. Oceans 97 (C5), 7305–7316. https://doi.org/10.1029/92JC00407.

Tan, H., Cai, H., Guo, Z., 2023. Increasing compound hazard of landfalling tropical cyclones in China during 1980–2020. Int. J. Climatol. 43. https://doi.org/10.1002/joc.8296.

Vincent, E.M., Lengaigne, M., Madec, G., Vialard, J., Samson, G., Jourdain, N.C., et al., 2012a. Processes setting the characteristics of sea surface cooling induced by tropical

cyclones. J. Geophys. Res. Oceans 117 (C2). https://doi.org/10.1029/2011JC007396.

Vincent, E.M., Lengaigne, M., Vialard, J., Madec, G., Jourdain, N.C., Masson, S., 2012b. Assessing the oceanic control on the amplitude of sea surface cooling induced by tropical cyclones. J. Geophys. Res. Oceans 117 (C5). https://doi.org/10.1029/2011JC007705.

Wang, G., Wu, L., Johnson, N.C., Ling, Z., 2016. Observed three-dimensional structure of ocean cooling induced by Pacific tropical cyclones. Geophys. Res. Lett. 43 (14), 7632–7638. https://doi.org/10.1002/2016GL069605.

Watanabe, M., Hibiya, T., 2002. Global estimates of the wind-induced energy flux to inertial motions in the surface mixed layer. Geophys. Res. Lett. 29 (8), 61–64. https://doi.org/10.1029/2001GL014422.

Wu, C., Lee, C., Lin, I., 2007. The effect of the ocean eddy on tropical cyclone intensity. J. Atmos. Sci. 64 (10), 3562–3578. https://doi.org/10.1175/JAS4051.1.

Wu, C.R., Chang, Y.L., Oey, L.Y., Chang, C.W.J., Hsin, Y.C., 2008. Air-sea interaction between tropical cyclone Nari and Kuroshio. Geophys. Res. Lett. 35 (12). https://doi.org/10.1029/2008GL033942.

Xu, Z., Yin, B., Hou, Y., Xu, Y., 2013. Variability of internal tides and near-inertial waves on the continental slope of the northwestern South China Sea. J. Geophys. Res. Oceans 118 (1), 197–211. https://doi.org/10.1029/2012JC008212.

Yang, B., Hou, Y., Hu, P., Liu, Z., Liu, Y., 2015. Shallow ocean response to tropical cyclones observed on the continental shelf of the northwestern South China Sea. J. Geophys. Res. Oceans 120 (5), 3817–3836. https://doi.org/10.1002/2015JC010783.

Ying, M., Zhang, W., Yu, H., Lu, X., Feng, J., Fan, Y., et al., 2014. An overview of the China meteorological administration tropical cyclone database. J. Atmos. Ocean. Technol. 31 (2), 287–301. https://doi.org/10.1175/JTECH-D-12-00119.1.

Zhang, H., He, H., Zhang, W., Tian, D., 2021. Upper ocean response to tropical cyclones: a review. Geosci. Lett. 8 (1). https://doi.org/10.1186/s40562-020-00170-8.

Zhang, Y., Liu, Y., Guan, S., Wang, Q., Zhao, W., Tian, J., 2023. Sudden track turning of typhoon prapiroon (2012) enhanced the upper ocean response. Remote Sens. 15 (2), 302. https://doi.org/10.3390/rs15020302. -Basel.

Zhao, Z., Alford, M.H., MacKinnon, J.A., Pinkel, R., 2010. Long-range propagation of the semidiurnal internal tide from the hawaiian ridge. J. Phys. Oceanogr. 40 (4), 713–736. https://doi.org/10.1175/2009JPO4207.1.

Zheng, M., Zhang, Z., Zhang, W., Fan, M., Wang, H., 2023. Effects of ocean states coupling on the simulated super typhoon Megi (2010) in the South China Sea. Front. Mar. Sci. 10.

Zhu, T., Zhang, D., 2006. The impact of the storm-induced SST cooling on hurricane intensity. Adv. Atmos. Sci. 23 (1), 14–22. https://doi.org/10.1007/s00376-006-0002-9.